

Nonlinear THz-Nano Metasurfaces

Tian Dong, Shaoxian Li, Manukumara Manjappa, Peidi Yang, Jiangping Zhou, Deyin Kong, Baogang Quan, Xieyu Chen, Chen Ouyang, Fei Dai, Jianguang Han, Chunmei Ouyang, Xueqian Zhang, Junjie Li, Yang Li, Jungang Miao, Yutong Li, Li Wang, Ranjan Singh,* Weili Zhang,* and Xiaojun Wu*

Extreme terahertz (THz) science and technologies, the next disruptive frontier in nonlinear optics, provide multifaceted capabilities for exploring strong light-matter interactions in a variety of physical systems. However, current techniques involve the need for an extremely high-field free space THz source that is difficult to generate and has limited investigations to a rather weak and linear regime of light-matter interactions. Therefore, new approaches are being sought for the tight confinement of THz waves that can induce nonlinear effects. Here, a nonlinear “tera-nano” metasurface is demonstrated exhibiting extremely large THz nonlinearity and sensitive self-modulation of resonances at moderate incident THz field strengths. A record deep-subwavelength ($\approx \lambda/33\ 000$) confinement of strongly enhanced (≈ 3200) THz field in a nano-gap (15 nm) exhibits remarkable THz field-tailored nonlinearity. Further, ultrafast injection of photocarriers reveals a competition between nonlinear THz field-induced intervalley scattering and optically driven interband excitations. The results on “tera-nano” metasurfaces enable a novel platform to realize enhanced nonlinear nano/micro composites for field-sensitive extreme THz nonlinear applications without the need for intense THz light sources.

1. Introduction

Field-sensitive nonlinearity^[1–3] and light-wave electronics^[4,5] are fascinating research topics that reveal exotic physical processes and hidden phases of matter in the presence of intense electromagnetic field excitation. Particularly, intense terahertz (THz) fields with low photon energy and picosecond time resolution offer a unique and powerful tool in manipulating relativistic electrons and in discovering novel physical aspects in photonics and condensed matter systems.^[6–13] With the maturity of femtosecond laser technology, intense THz sources based on tilted pulse front technology,^[14–16] organic crystal,^[17] photoconductive antenna,^[8] and transition radiation^[18] have now become accessible with peak electric fields greater than MV cm^{-1} . These efforts have led to the recent rapid development of strong nonlinear physics at THz frequencies

T. Dong, P. D. Yang, J. P. Zhou, D. Y. Kong, Prof. F. Dai,
Prof. J. G. Miao, Prof. X. J. Wu
School of Electronic and Information Engineering
Beihang University
Beijing 100083, China
E-mail: xiaojunwu@buaa.edu.cn

S. X. Li, X. Y. Chen, Prof. J. G. Han, Prof. C. M. Ouyang,
Prof. X. Q. Zhang, Prof. W. L. Zhang
Center for THz Waves and College of Precision Instrument
and Optoelectronics Engineering, and the Key Laboratory
of Optoelectronics Information and Technology
Tianjin University
Tianjin 300072, China
E-mail: weili.zhang@okstate.edu

M. Manjappa, Prof. R. Singh
Division of Physics and Applied Physics
School of Physical and Mathematical Sciences
Nanyang Technological University
21 Nanyang Link, Singapore 637371, Singapore
E-mail: ranjans@ntu.edu.sg

 The ORCID identification number(s) for the author(s) of this article can be found under <https://doi.org/10.1002/adfm.202100463>.

M. Manjappa, Prof. R. Singh
Centre for Disruptive Photonic Technologies
The Photonics Institute
Nanyang Technological University
50 Nanyang Avenue, Singapore 639798, Singapore
Prof. B. G. Quan, C. Ouyang, Prof. J. J. Li, Prof. Y. T. Li, Prof. L. Wang
Beijing National Laboratory for Condensed Matter Physics
Institute of Physics
Chinese Academy of Sciences
Beijing 100190, China
Prof. Y. Li
State Key Laboratory of Precision Measurement
Technology and Instrument
Department of Precision Instrument
Tsinghua University
Beijing 100084, China
Prof. W. L. Zhang
School of Electrical and Computer Engineering
Oklahoma State University
Stillwater, OK 74078, USA
Prof. X. J. Wu
Wuhan National Laboratory for Optoelectronics
Huazhong University of Science and Technology
Wuhan 430074, China

DOI: 10.1002/adfm.202100463

that host the testing bed for a multitude of novel physical phenomena and collective states of matter in a variety of solid-state and condensed matter systems. In graphene and other topological Dirac materials, THz nonlinearity has been shown via the generation of higher-order harmonics induced by the tightly focused intense THz pulse with a peak electric field of few MV cm⁻¹.^[19,20] In strongly correlated matter systems, high-frequency resonance phenomena and collective hidden phases of matter are revealed by pumping with ultra-strong THz fields.^[21–23] Further, the advent of THz-pump/THz-probe techniques has enabled to probe various interaction dynamics in nonequilibrium-driven states of classical and quantum material systems.^[24–26] The nonlinear THz physics offers immense potential in fundamental science and technological innovations, however, so far these investigations are majorly limited to the bulk/macroscopic scale of light-matter nonlinearity with extremely intense incident THz fields higher than MV cm⁻¹. Owing to the fundamental significance and exciting prospects, there is a strong interest and need to realize more reliable devices and materials platforms to enable extreme THz nonlinearity at the micro/nanoscale for driving the efficacy of field-sensitive nonlinearities without the need for intense incident fields.

The subwavelength electromagnetic metamaterials/metasurfaces provide a promising route to localize and enhance the field strengths within the micro/nano spatial regimes that aim to provide enhanced nonlinear micro/nanocomposites across frequencies.^[27,28] Particularly, reconfigurable metasurfaces^[29–34] are attracting a lot of interest to dynamically tune the frequency, phase, and amplitude of the incident waves. In recent years, strong THz-field induced nonlinear reconfigurable metasurfaces have also emerged as sensitive and tunable devices for their field-sensitive effects and active reconfigurability. In these systems, the effect of THz nonlinearity has been either shown via field-induced phase transition in materials such as VO₂, or through a strong scattering of free carriers within the semiconductor substrates.^[35–37] These demonstrations rely on nearly 20-fold enhancement in a microscale spatial confinement of the THz field that still requires excitation of the samples with intense THz pulses (field strength of few hundred kV cm⁻¹ to MV cm⁻¹) to observe nonlinear effects. A more promising approach is to engineer and amplify the tightly confined spatial fields in the metamaterial structures to tailor and enhance the system nonlinearity under the regime of low-intensity THz fields.^[38–41]

Here, for the first time, we demonstrate a “tera-nano” metasurface showing extreme THz nonlinearity and sensitive self-modulation of resonances. Inspired by the semiconductor field-effect devices, we enhance the field strength by four orders of magnitude in a tera-nano metasurface through nano-scale confinement of THz fields by shrinking its capacitive gaps down to 15 nm ($\approx \lambda/33\ 000$). The nano-gaps are switched ON/OFF using THz fields of contrasting strengths owing to the carrier multiplication effects caused by giant local THz electric field confined in the nano-gap region, thereby enabling nonlinear and field-sensitive resonance switching. This demonstrates dynamical reconfiguration of the metasurface resonance using incident THz fields of moderate strengths of less than 60 kV cm⁻¹ that eliminates the need for high intense THz fields

(>100 kV cm⁻¹). These results provide promising direction in developing efficient nonlinear composites for realizing extreme THz nonlinearity and enhanced light-matter interactions in the nano/microscale systems.

2. Results and Discussions

2.1. THz-Nano Metasurface and Field Enhancement

The demonstrated tera-nano metasurface consists of a square array of gold split ring resonators (SRRs) with 15-nm gaps fabricated on a silicon substrate as shown in **Figure 1a**. In the presence of THz fields in the nano-gaps enables extreme local field enhancement that results in the efficient carrier multiplication effect in the gaps. As a result, the silicon interacts with an extreme field, giving rise to a nonlinear increase of the local conductivity, thus making the single-nanogap SRRs (SN-SRRs) and double-nanogap SRRs (DN-SRRs) comparable to the closed-ring resonators (CRRs) in terms of geometry. In order to elucidate the record local field enhancement capability of nanogap SRRs, we perform numerical simulations by shrinking the gap size (g) from microns ($g = 5\ \mu\text{m}$) scale to the order of nanometers ($g = 5\ \text{nm}$), as can be seen in **Figure 1b**. When the gap size is 5 μm , the field enhancement factor β is ≈ 3 at 0.22 THz for the electric field polarized along the arm with a gap (TM polarization). As the gap size reduces to 15 nm, β increases to ≈ 3200 and it can be further increased to $\approx 18\ 000$ when the gap size decreases to 5 nm. Even at the non-resonant frequencies, the field enhancement factor can be increased for nearly three orders of magnitude by decreasing the gap size to 5 nm. Here we choose to monitor the field enhancement factor at 0.22 THz to match the maximum spectral density of the THz pulse emitted from the LiNbO₃ (See the inset of **Figure S1b**, Supporting Information). On the other hand, we use asymmetric DN-SRRs structure as it supports the excitation of sharp Fano resonance^[42,43] that constitutes a strong enhancement in the THz field confinement in the nano-gaps. These Fano resonances result from the interference mechanisms between the asymmetric resonators, therefore, enhancing its nonlinear and sensitive performance owing to its much higher Q-factor and strong field-confinement. Such a strong local field enhancement at the gap region provides an effective way to amplify the local nonlinear effects to switch the resonance properties of the metasurface. Additionally, we show the corresponding field distributions around the gap area for different gap sizes in **Figure 1c–e**. The smaller the gap size, the higher the electric field density around the gap area.

2.2. Sample Preparation and Characterization

The metasurface design with $g = 15\ \text{nm}$ in **Figure 1a** is then fabricated using conventional lithography techniques combined with tilting sample method to realize the nano-gaps in the micron-sized SRRs (Experimental Section). The scanning electron microscope (SEM) image of the SN-SRRs is presented in **Figure 2a**, which shows the square array of the SRRs consisting of gold structures with nano-gap width of $g = 15\ \text{nm}$ on a 0.5-mm-thick high-resistivity silicon substrate. The periodicity

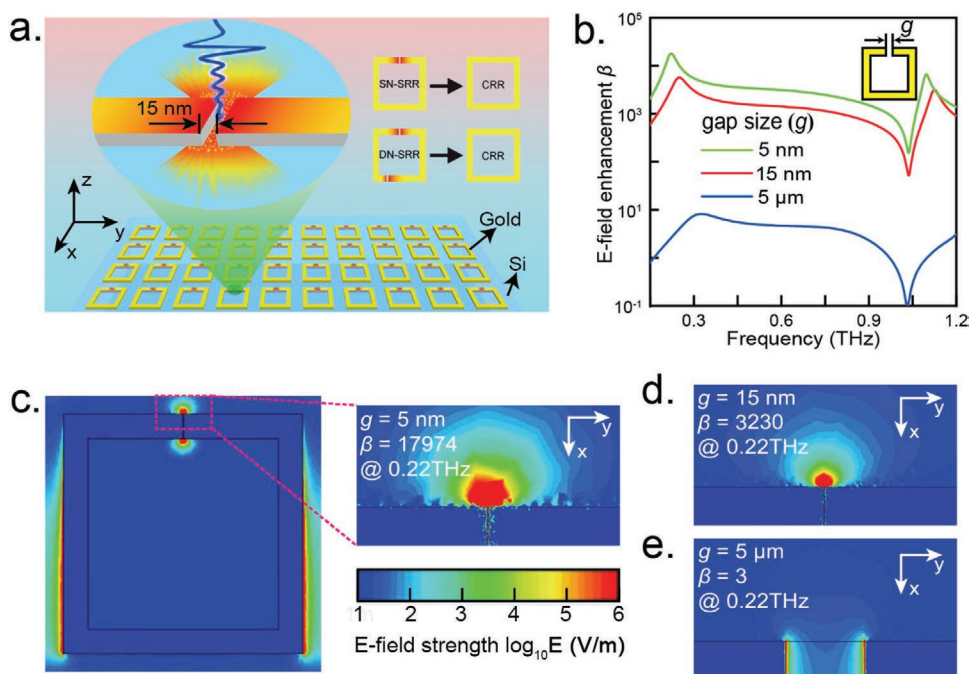


Figure 1. Schematic diagram of the metasurfaces and comparison between SN-SRRs, DN-SRRs, and CRRs. a) The metasurface consists of a square array of gold CRRs/nanogap-SRRs with silicon as a substrate. When the normal incident THz wave is illuminated onto the metasurface, several carriers will populate the nanogap area because of cascaded impact ionization induced by an ultra-high local electromagnetic field. This leads to the equivalent closing of the nanogap, making the SN-SRRs and DN-SRRs become like the CRRs. b) Electric field enhancement spectra averaged over the gap volume for gap sizes g of 5 μm , 15 nm, and 5 nm, respectively. For nanogaps with 15 and 5 nm, the field enhancement factors can reach up to several thousand times for the frequency range <1.0 THz. Corresponding field distribution at 0.22 THz in the vicinity of the gap for gap width c) $g = 5$ nm, d) $g = 15$ nm, and e) $g = 5 \mu\text{m}$. SRRs with a smaller gap size have led to tighter confinement of electromagnetic energy.

of a square unit cell is 69 μm , at the center of which is the gold ring with a length of 47 μm , a width of 6 μm , and a thickness of 80 nm. To measure the resonant properties of the SN-SRRs metasurface, we use a THz time-domain spectrometer (THz-TDS) to characterize the samples.^[44] Here, TE and TM polarizations correspond to the electric field polarized in perpendicular and parallel direction to the gap bearing arm of the resonator, respectively (Figure 2b). For sample characterization, we measured the transmission spectra of SRR structures with one and two nano-gaps as well as CRRs for TM and TE polarizations. Figure 2c shows SN-SRRs' transmission spectrum with TE and TM-polarized weak THz field. For TM-polarized transmission, there are three resonant modes, reading as $f_1 = 0.24$ THz ($m = 1$, LC mode), $f_2 = 0.81$ THz ($m = 3$, quadruple mode), and $f_3 = 1.10$ THz (diffractive mode). The most pronounced quadruple resonance locates at $f_2 = 0.81$ THz with a minimum transmission down to 7%, while that for both f_1 and f_3 are 45 and 35%, respectively. In the case of TE polarization, the resonance frequency locates at ≈ 0.69 THz ($m = 2$, dipole mode), exhibiting a frequency redshift of 120 GHz from the TM polarization's case.

To confirm the fact that the field enhancement factor and the frequency shift can be enhanced with the number of nanogaps, we fabricated and characterized the DN-SRRs with designed asymmetry (asymmetry parameter $\alpha = 12.5\%$)^[45] and two nano-gaps ($g = 15$ nm) on separate arms.^[46] As shown in Figure 2d, the resonant frequencies of corresponding $m = 2$ and $m = 3$ modes are at 0.69 and 0.92 THz, respectively, for TE and TM

excitations. The resonance frequency shift is 230 GHz, almost twice as that of SN-SRRs. Here the geometric parameters of DN-SRRs are the same as those of SN-SRRs except for it consists of two nano-gaps on the opposite arms. The second arm is located one quarter away from the end of the arm to achieve an asymmetry (asymmetry parameter $\alpha = 12.5\%$) between these two gaps. For CRRs (Figure 2e), the resonant frequency for both TE and TM polarizations are located at ≈ 0.70 THz because of its fourfold rotational symmetry. Experimental results are in good agreement with the simulated transmission spectra shown in Figure 2f–h, thereby confirming the twofold enhancement of frequency shift for DN-SRRs when compared with SN-SRRs.

2.3. Strong THz Field Induced Nonlinear Frequency Modulation

To observe THz-field sensitive nonlinear behavior, we generate THz pulses with electric field amplitude of ≈ 100 kV cm^{-1} via tilted pulse front technique using lithium niobate crystals (Figure 3a). Using a lithium niobate THz source with a moderate intensity ≈ 100 kV cm^{-1} peak field strength, we cannot generate a nonlinear response on a blank high-resistivity silicon wafer (Section S5, Supporting Information), which requires field strengths greater than MV cm^{-1} . However, a nonlinear response could be generated with moderate THz intensities in silicon by fabricating SN-SRRs or DN-SRRs metasurfaces with nano-gaps, showing homogeneously enhanced localized field effects inside their nano-gap region. As shown in Figure 3b,

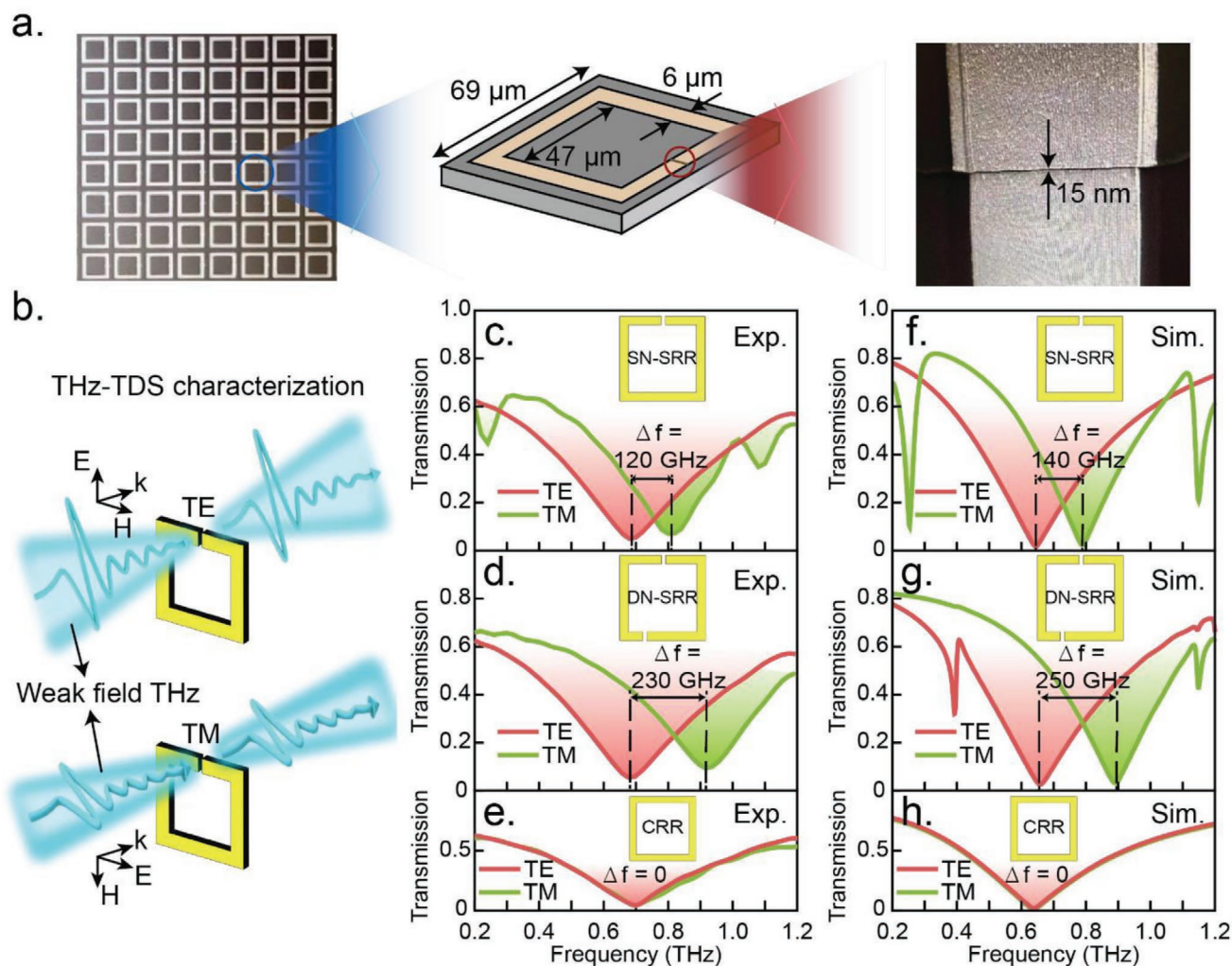


Figure 2. Fabrication and characterization of nano-gap SRR metasurfaces. a) SEM images of SN-SRR metasurface with a period of $69\ \mu\text{m}$. The square gold ring has an inner side length of $47\ \mu\text{m}$ and a width of $6\ \mu\text{m}$. The thickness of the substrate and the gold ring resonator is $500\ \mu\text{m}$ and $80\ \text{nm}$, respectively. Confirmed by SEM, THz time-domain spectroscopy and CST simulations, the SRR nanogap size is $15\ \text{nm}$. b) Schematic diagram of two different polarizations of the incident wave. TE and TM polarization correspond to electric field perpendicular and parallel to the gap-bearing arm, respectively. c–e) Three types of metasurfaces have the same resonant frequency under TE polarization, but in the case of TM polarization, SN-SRR metasurface exhibits $120\ \text{GHz}$ frequency shift while DN-SRR metasurface shows a larger frequency shift of $230\ \text{GHz}$. f–h) Simulation results calculated by the commercially available CST microwave studio.

an SN-SRRs metasurface switches resonance frequencies from ≈ 0.76 to $0.68\ \text{THz}$, when the incident THz field strength is increased from 2 and $100\ \text{kV cm}^{-1}$, respectively, featuring a nonlinear frequency redshift of $80\ \text{GHz}$. Such a nonlinear self-frequency modulation behavior is caused by the strong local field enhancement provided by the nanogaps of SRRs. When the THz field strength is weak ($2\ \text{kV cm}^{-1}$), the nanogap is equivalent to disconnected metal wires, indicating an “OFF” state. On increasing the THz field strength to $100\ \text{kV cm}^{-1}$ significantly enhances the carrier multiplication effect in the nanogaps, thereby increasing the conductivity of the silicon substrate dramatically leading to nonlinear self-modulation of frequency and amplitude of the resonance. Such an SRR with a high conductivity nanogap is structurally equivalent to a CRR, as illustrated in the inset of Figure 1a, leading to the dipole resonance and an “ON” state for the nonlinear switching. For

the DN-SRR metasurface, the resonant frequency shifts from ≈ 0.84 to $0.67\ \text{THz}$, when the THz field strength increases from 2 to $100\ \text{kV cm}^{-1}$ (Figure 3c) that corresponds to a frequency redshift of $170\ \text{GHz}$. As a comparison, the resonant frequencies of CRRs for different field intensities (Figure 3d) show that CRRs do not have THz nonlinear self-frequency modulation behavior due to the absence of nanogap and local field enhancement. Furthermore, we analyzed the resonant frequencies while continuously varying the field intensity for three structures as plotted in Figure 3e. In the case of SN-SRRs, as the field strength increases, the resonant frequency first exponentially decays, and then saturates near the fluence of $\approx 60\ \text{kV cm}^{-1}$. On the other hand, the saturation effect for the frequency shift can be reached at much lower THz strengths ($\approx 40\ \text{kV cm}^{-1}$) for DN-SRRs with two nano-gaps. According to these results, we can calculate the relaxation constants of SN-SRRs and DN-SRRs as

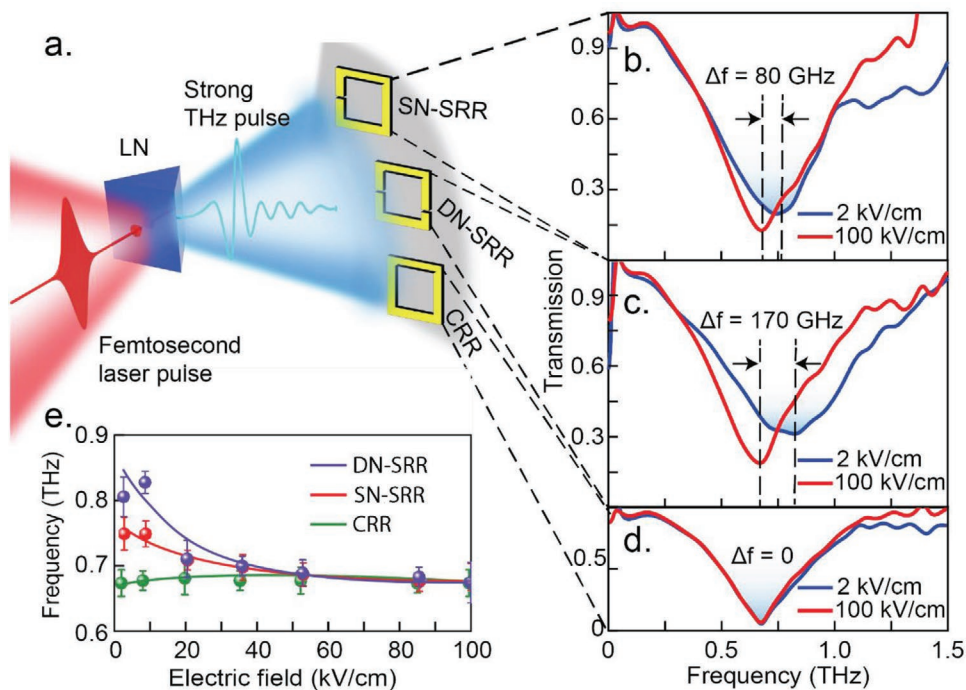


Figure 3. Strong field THz induced nonlinear frequency tuning. a) The strong field THz pulse is generated via tilted wavefront technology in a lithium niobate crystal, and then is illuminated onto three different types of metasurfaces. Measured normalized transmitted spectra for b) SN-SRRs, c) DN-SRRs, and d) CRRs under 2 and 100 kV cm⁻¹ THz illuminations. The SN-SRR sample exhibits 80 GHz frequency shift when the incident field is switched from 2 to 100 kV cm⁻¹, while for the DN-SRR sample, the frequency shift is 170 GHz, almost twice as the SN-SRR case. There is no frequency shift for the CRR case due to the lack of nanogap manipulation. e) THz field-dependent nonlinear resonant frequency shift. The frequency shifts of both DN-SRR and SN-SRR decrease exponentially with the increase of the electric field amplitude. However, CRR does not show apparent correlations with the incident field.

18 and 30, respectively. The much faster decay rate provided by the DN-SRRs implies the fact that the collective field enhancement factor and the degree of frequency shift are proportional to the number of nanogaps.

To further analyze this fact, simulations are performed using rings with multiple nanogaps to establish the dependence of the degree of nonlinear frequency shift on the number of nano-gaps in SRRs. As shown in Figure 4a, the resonant frequencies at 2 and 100 kV cm⁻¹ coincide for CRRs. When we increase the gap number to $n = 1$, the difference in the resonant frequencies is 146 GHz (Figure 4b). It further increases to 233 GHz when the number of gaps increases to $n = 2$ as illustrated in Figure 4c. The frequency shift with the increasing number of nanogaps is summarized in Figure 4d. The increase in the frequency shift is a result of the average collective response from all the nano-gaps in the unit cell structure, which is a signature of collective nonlinearity in the frequency shift of the far-field resonance. The collective nonlinearity sustains till the number of nano-gaps increases to $n = 5$, showing a finite change in the frequency shift of the resonance. As the number of gaps further increase ($n > 5$), the frequency shift shows a saturation effect that reaches a total shift of 400 GHz, after which the nonlinearity ceases to exist. This effect signifies the saturation in the local field enhancement with respect to the number of nano-gaps, which is due to the onset of mutual interactions between the localized fields of nearby nano-gaps, as the separation between the gaps

is decreased with increasing the gap numbers. In addition to the frequency modulation, variation of the incident THz fields can also induce changes in the phase of the transmission for over 20° and 40° around the resonant frequency, for SN-SRRs and DN-SRRs respectively (Section S6, Supporting Information).

In our experiments, although the THz field magnitude is no more than 100 kV cm⁻¹, the local field in the nanogap can be enhanced higher than 100 MV cm⁻¹, which is sufficient to induce impact ionization.^[35] Since the relaxation time of impact ionization is much shorter than the duration of THz pulse (hundreds of fs), impact ionization happens in a cascaded manner during each THz pulse shot, generating a large number of free charge carriers. Hence, the carrier concentration of silicon in the nanogap can increase by 10 orders of magnitude (Section S7, Supporting Information), thus closing the nanogap and leading to a shift in the resonant frequency. To confirm the fact that the extremely strong local-field enhancement provided by the nanogap is necessary for the cascaded impact ionization, we also measure the transmission through single-microgap SRRs (SM-SRRs) whose gap size is $g = 5 \mu\text{m}$ under different strengths of THz fields (Section S8, Supporting Information). Results show that switching THz field magnitudes from 2 to 100 kV cm⁻¹ does not alter the resonant frequency and amplitude of SM-SRRs that highlights the absence of nonlinear effect in the micro-gap structures.

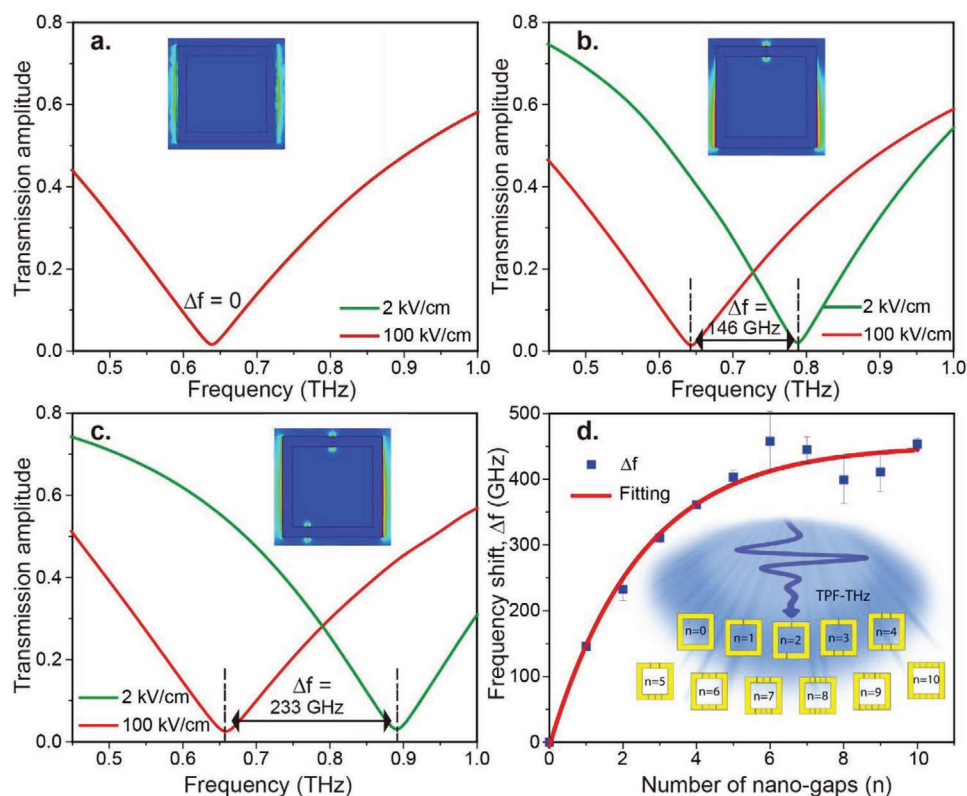


Figure 4. Nonlinear self-frequency modulation with an increasing number of nanogaps. The simulated resonance frequency shift of SRRs with a) closed-ring, b) one gap, and c) two gaps, with corresponding frequency shift (Δf) of 0, 146, and 233 GHz, respectively. d) The saturation effect of the frequency shift (Δf) with varying numbers of nano-gaps in the structure. The variation in Δf is fitted (red curve) with the exponential function e^{Rx} , where “R” is the rate constant and “x” is the variable.

2.4. Optical Reconfiguration of Resonances in Nonlinear THz-Nano Metamaterial

To further elucidate the observed THz nonlinear self-modulation effects are due to carrier multiplication via a strong THz field, we perform carrier multiplication by photodoping the silicon substrate using an optical pulse (Figure 5a). In order to shrink the interplay volume, and obtain a striking nonlinear phenomenon, we used a BBO generated optical pump pulse of wavelength 400 nm, then injected electrons from the valence band to L-valley via interband transitions, leading to excess carrier density of $\approx 1.4 \times 10^{19} \text{ cm}^{-3}$ (under pump fluence of $\approx 70 \mu\text{J cm}^{-2}$). Due to the screening effect by the generated free carriers, the impact ionization is strongly-correlated with initial carrier density,^[45] which can be significantly weakened in our context. Therefore, the intervalley and Auger recombination will dominate the physical process under optical injection. Figure 5c–e shows the THz transmission spectra of SN-SRRs, DN-SRRs, and CRRs first illuminated by an optical pump and then a weak or strong THz pulse. In all three cases, the strength of the resonance decreases in the presence of the optical pump. This is due to the uniform distribution of the optically injected photocarriers over the silicon substrate that increases the overall carrier density and the corresponding conductance, thereby decreasing the strength of the resonance induced by the geometry of the metallic resonator. Compared to the weak THz field illumination, the strong THz field results

in resonances with higher quality factors and smaller frequency blueshifts after the 400-nm pump. Such a phenomenon is a result of intervalley scattering and Auger recombination. As shown in Figure 5b, the strong THz field induces intervalley scattering of carriers in the conduction band, leading to a pronounced reduction of the carrier mobility and substrate conductivity, thus counteracting the optically injected photocarriers and enhancing the geometry-induced resonance (Section S10, Supporting Information). As a secondary and minor contribution compared with intervalley scattering, Auger recombination induced by the strong THz field depletes the optically injected photocarriers, especially in the silicon at the nanogap region.^[47,48] This reduces the conductivity of the silicon in the nanogap, and in turn mitigates the suppression of amplitude of SRR resonances induced by the optical pump. Such a phenomenon appears for all ring-resonator-based metasurfaces with or without nano-/micro-gaps under both weak and strong THz fields, indicating that the optically injected photocarriers predominate the counter effect induced by the THz field via intervalley scattering and Auger recombination. Compared to the THz modulation induced by optical photodoping; the metasurface-based THz nonlinear self-modulation has several unique advantages. First, THz field-induced nonlinear self-modulation can tune the THz property of any desired area by fabricating well-controlled SRRs and second, it does not require an additional optical pump. These techniques allow the realization of enhanced THz nonlinearities using micro/nanocomposites,

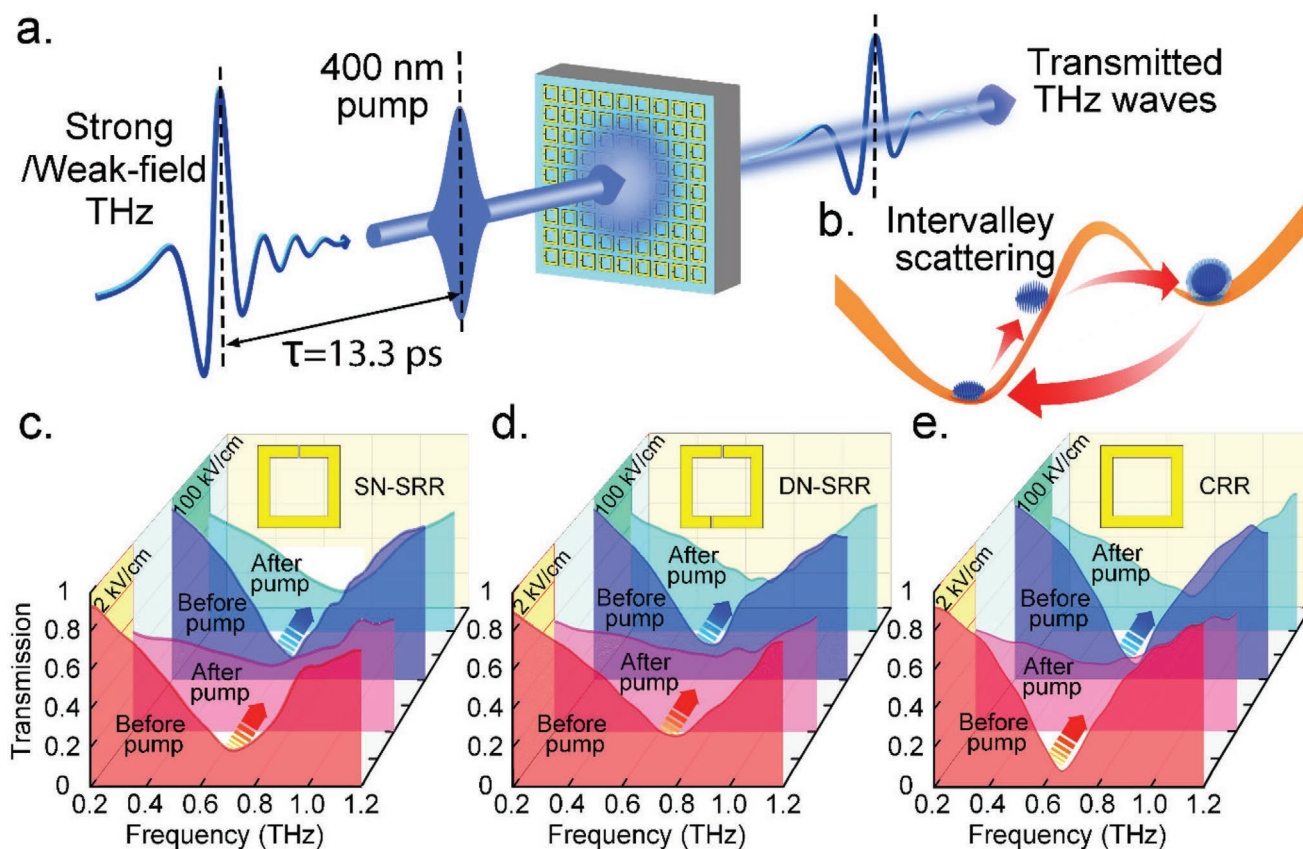


Figure 5. Impact of photodoping on nonlinear THz responses. a) Schematic diagram of 400 nm pump THz probe system. The THz wave is illuminated onto the metasurface 13.3 ps after the 400 nm pump. b) Intervalley scattering occurs after the illumination of a strong THz wave, decreasing the mobility of the electrons. (c–e) Measured THz transmission spectra for c) SN-SRRs, d) DN-SRRs, and e) CRRs with the 400 nm pump power of 6.19 mW at 2 and 100 kV cm⁻¹ THz field strengths, respectively.

thereby creating a novel platform for extreme light-matter interactions and energy-efficient active reconfigurable photonic devices across frequencies.

3. Conclusion

We demonstrated active reconfigurable nonlinear tera-nano metasurfaces showing strong THz nonlinearity and field-induced self-modulation effects at moderate strengths of incident THz field lower than 60 kV cm⁻¹. The fabricated SRRs with nano-gaps of 15 nm enabled strong field localization and enhancement of 10⁴ times leading to the nonlinear field-induced carrier multiplication in silicon substrate. We also investigated the fact that a strong THz field can mitigate the density of photocarriers injected by optical pump via intervalley scattering and Auger recombination. Our reconfigurable tera-nano metasurfaces can serve as a platform for exploring ultra-strong THz-matter interactions^[25] with potential applications in nonlinear frequency switches, high-sensitivity bio-/environmental sensing,^[49] beam steering,^[50] high-resolution imaging,^[51] next-generation wireless communications and networking,^[52] THz computations,^[53] and to explore the novel local-nonlinear effects in material systems without the need for intense THz light sources.

4. Experimental Section

Confirming the Nanogap Size: Fabrication of large-area splitting resonators with nano-scale gaps required excellent fabrication techniques. To ensure the correctness of the experimental results, it was necessary to verify whether the samples have been fabricated successfully. To this end, the SN-SRR sample by a homemade THz-TDS system was first characterized, thus obtaining the transmission curves of TM and TE incident THz electric fields and recorded the resonant frequencies of the two cases. Then the size of the gap was scanned in the commercially available Computer Software Technology (CST) microwave studio, and the gap size was recorded when the simulation resonance frequency and the THz-TDS-obtained resonance frequency coincide. It was found that the simulation size value was very close to 15 nm, preliminarily confirming the success of the sample processing. Next, the same procedures were conducted on the asymmetric DN-SRR sample. When the size of the scanning gap was close to 15 nm, the same result can be achieved as that of THz-TDS measurement, which further indicated that the gap size was 15 nm. This validation was essential and necessary because it provides a correct premise for the subsequent experiments and the discussion of the results.

THz Generation in a Lithium Niobate Crystal: A commercial femtosecond laser amplifier (Coherent) was employed as a pump source for the nonlinearity experiments, which has a central wavelength of 800 nm, a pulse width of 30 fs, a repetition rate of 1 kHz, and a maximum single pulse energy of 7 mJ. A grating with 1500 lines mm⁻¹ with a maximum diffraction efficiency of ≈85% for -1 order was used for tilting the pump pulse intensity. A half-wave plate was to rotate the horizontally polarized pump pulses to vertical,

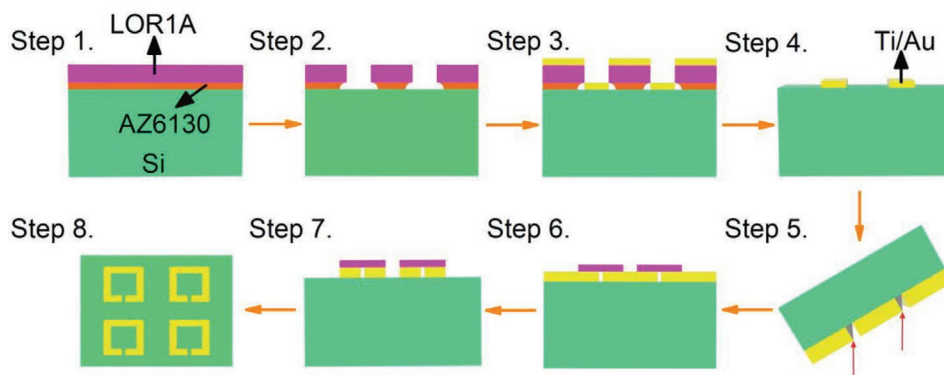


Figure 6. The specific illustration of fabrication procedures. In the first step, photoresist LOR1A and AZ6130 are spin-coated onto the surface of the intrinsic silicon substrate, respectively, and then we perform lithography to shape the pattern of the nano-gaps. In the developing step (Step 2), more parts of the photoresist in the bottom are etched to reduce the hindrance to the formation of the metal edge using electron beam evaporation (Step 3). Here we add one Ti layer below the Au layer to increase the adhesion of gold to silicon. In Step 4, we use a developer AZ300MIF to strip the photoresist. In the next step, before evaporating the rest of the metals, the sample is first tilted for a specific angle, thus making it easier to form the nano-gaps. The total thickness of the Ti and Au are 10 and 80 nm, respectively. Then we perform spin coating and photolithography development again in Step 6 and Step 7 to obtain the pattern of the metal rings. Finally, ion beam etching and cleaning are conducted in Step 8, and thus the SRRs are successfully fabricated on the silicon substrate.

and then the pump pulses were imaged into a z-cut lithium niobate crystal with a triangle shape. The crystal was not cryogenically cooled resulting in the generation of 0.3 THz peak frequency and 0.1–1.0 THz frequency range due to a higher linear absorption coefficient for the generated THz waves inside the crystal. The outcoupled THz wave was first reflected by an aluminum mirror and then collimated by a 90° off-axis parabolic mirror. Two THz polarizers were inserted into the collimated THz beam to vary the THz intensity for nonlinearity experiments. After the second parabolic mirror, the strong THz field pulses were focused onto the nanogap metasurfaces, and the transmitted signals were collected by another two parabolic mirrors and then diagnosed by EOS. Before measurements, the THz field strengths were calibrated by a commercial pyroelectric detector (Gentec) and EOS, and verified the maximum THz field strength pumped at ≈ 3 mJ was ≈ 100 kV cm⁻¹.

400 nm Pump-Strong THz Field Probe Technique: To investigate the influence of the photodoped carriers on the THz nonlinearity in nanogap metasurfaces, 400 nm pump pulses were generated in a BBO crystal. Another delay line was added to vary the time delay between the 400 nm and THz pulses for pump-probe experiments. The generated 400 nm light together with the residual 800 nm pulses were divided by a dichroic mirror, in which the 400 nm pulses were reflected while the residual 800 nm light was transmitted. After reflecting by a pellicle which was transmitted for THz pulses, the 400 nm pump pulses and THz waves were spatially focused onto the samples. 400 nm pump pulses could inject considerable carriers directly into high resistivity silicon substrates resulting in the disturbance of THz nonlinearity in nanogap metasurfaces. In addition, this system has the ability of alternating THz probe. By comparing the difference between the photogenerated carriers and the THz self-induced nonlinear response, the mechanism of different generation modes of photogenerated carriers on the nonlinear modulation of THz wave was clarified. This kind of experimental device has high requirements on light path construction, time synchronization, and experimental techniques, so two delay lines were used to study time-resolved dynamics.

Fabrication of Nanogap Metasurfaces: To fabricate the nanogap metasurfaces, nano-scale gaps were fabricated first, and then calibrated metal rings. When processing the nanogaps, the photoresist was spin-coated on the intrinsic silicon substrates. The type of the upper and lower photoresist layers was LOR1A and AZ6130, respectively, and then striping patterns of gaps were formed via lithography. The second step was photolithography development. In this step, the two sides of the structure were intentionally designed to be concave, which avoided burrs in the metal corner produced in the next step. In the third step,

electron beam evaporation was carried out where Ti and Au were coated successively. Degumming comes as the fourth step which focused on stripping the photoresist and LOR1A using a developer called AZ300MIF. Next, when evaporating metals, the sample was first tilted for a specific angle, which made it easier to form the nanogaps, and then 80 nm thick Au and 10 nm thick Ti were evaporated onto the surface. Then, spin-coating and photolithography development were carried out in the same process as the fabrication of nanogaps as illustrated in Steps 6 and 7 of Figure 6. Finally, ion beam etching was conducted in the eighth step to etch the extra metals. After cleaning the photoresist, the THz-Nano metasurfaces with an overall size of 1.5 cm × 1.5 cm were obtained.

Supporting Information

Supporting Information is available from the Wiley Online Library or from the author.

Acknowledgements

T.D., S.L., and M.M. contributed equally to this work. This work was supported by the National Natural Science Foundation of China (61905007, 11827807), the National Key R&D Program of China (2019YFB2203102), and the Open Project Program of Wuhan National Laboratory for Optoelectronics No. 2018WNL0KF001, and the Open Fund of Guangdong Provincial Key Laboratory of Information Photonics Technology (Guangdong University of Technology, No. GKPT20). M.M. and R.S. acknowledge research funding support from the Ministry of Education, Singapore (AcRF Tier 1, Grant RG191/17, MOE2017-T2-1-110, and MOE2016-T3-1-006(S)).

Conflict of Interest

The authors declare no conflict of interest.

Data Availability Statement

Data openly available in a public repository that issues datasets with DOIs.

Keywords

metasurfaces, nano-gaps, nonlinearity, strong-field terahertz

Received: January 16, 2021

Published online:

- [1] X. Li, T. Qiu, J. H. Zhang, E. Baldini, J. Lu, A. M. Rappe, K. A. Nelson, *Science* **2019**, 364, 1079.
- [2] G. Vampa, T. J. Hammond, M. Taucer, X. Ding, X. Ropagnol, T. Ozaki, S. Delprat, M. Chaker, N. Thiré, B. E. Schmidt, F. Légaré, D. D. Klug, A. Y. Naumov, D. M. Villeneuve, A. Staudte, P. B. Corkum, *Nat. Photonics* **2018**, 12, 465.
- [3] S. Chen, K. F. Li, G. Li, K. W. Cheah, S. Zhang, *Light: Sci. Appl.* **2019**, 8, 17.
- [4] X. Yang, C. Vaswani, C. Sundahl, M. Mootz, L. Luo, J. H. Kang, I. E. Perakis, C. B. Eom, J. Wang, *Nat. Photonics* **2019**, 13, 707.
- [5] E. J. Sie, C. M. Nyby, C. D. Pemmaraju, S. J. Park, X. Shen, J. Yang, M. C. Hoffmann, B. K. Ofori-Okai, R. Li, A. H. Reid, S. Weathersby, E. Mannebach, N. Finney, D. Rhodes, D. Chenet, A. Antony, L. Balicas, J. Hone, T. P. Devereaux, T. F. Heinz, X. Wang, A. M. Lindenberg, *Nature* **2019**, 565, 61.
- [6] G. Schmid, K. Schnorr, S. Augustin, S. Meister, H. Lindenblatt, F. Trost, Y. Liu, N. Stojanovic, A. Al-Shemmary, T. Golz, R. Treusch, M. Gensch, M. Kubel, L. Foucar, A. Rudenko, J. Ullrich, C. D. Schroter, T. Pfeifer, R. Moshhammer, *Phys. Rev. Lett.* **2019**, 122, 073001.
- [7] L. Luo, X. Yang, X. Liu, Z. Liu, C. Vaswani, D. Cheng, M. Mootz, X. Zhao, Y. Yao, C. Z. Wang, K. M. Ho, I. E. Perakis, M. Dobrowolska, J. K. Furdyna, J. Wang, *Nat. Commun.* **2019**, 10, 607.
- [8] X. Chai, X. Ropagnol, S. M. Raies-Zadeh, M. Reid, S. Safavi-Naeini, T. Ozaki, *Phys. Rev. Lett.* **2018**, 121, 143901.
- [9] L. Zhao, Z. Wang, H. Tang, R. Wang, Y. Cheng, C. Lu, T. Jiang, P. Zhu, L. Hu, W. Song, H. Wang, J. Qiu, R. Kostin, C. Jing, S. Antipov, P. Wang, J. Qi, Y. Cheng, D. Xiang, J. Zhang, *Phys. Rev. Lett.* **2019**, 122, 144801.
- [10] D. Zhang, A. Fallahi, M. Hemmer, X. Wu, M. Fakhari, Y. Hua, H. Cankaya, A. L. Calendron, L. E. Zapata, N. H. Matlis, F. X. Kärtner, *Nat. Photonics* **2018**, 12, 336.
- [11] C. Kealhofer, W. Schneider, D. Ehberger, A. Ryabov, F. Krausz, P. Baum, *Science* **2016**, 352, 429.
- [12] W. R. Huang, A. Fallahi, X. Wu, H. Cankaya, A.-L. Calendron, K. Ravi, D. Zhang, E. A. Nanni, K.-H. Hong, F. X. Kärtner, *Optica* **2016**, 3, 1209.
- [13] L. Wimmer, G. Herink, D. R. Solli, S. V. Yalunin, K. E. Echternkamp, C. Ropers, *Nat. Phys.* **2014**, 10, 432.
- [14] X. J. Wu, J. L. Ma, B. L. Zhang, S. S. Chai, Z. J. Fang, C. Y. Xia, D. Y. Kong, J. G. Wang, H. Liu, C. Q. Zhu, X. Wang, C. J. Ruan, Y. T. Li, *Opt. Express* **2018**, 26, 7107.
- [15] X. Wu, S. Carbajo, K. Ravi, F. Ahr, G. Cirmi, Y. Zhou, O. D. Mücke, F. X. Kärtner, *Opt. Lett.* **2014**, 39, 5403.
- [16] X. Wu, A. L. Calendron, K. Ravi, C. Zhou, M. Hemmer, F. Reichert, D. Zhang, H. Cankaya, L. E. Zapata, N. H. Matlis, F. X. Kärtner, *Opt. Express* **2016**, 24, 21059.
- [17] C. Vicario, A. V. Ovchinnikov, S. I. Ashitkov, M. B. Agranat, V. E. Fortov, C. P. Hauri, *Opt. Lett.* **2014**, 39, 6632.
- [18] G. Liao, Y. Li, H. Liu, G. G. Scott, D. Neely, Y. Zhang, B. Zhu, Z. Zhang, C. Armstrong, E. Zemaityte, P. Bradford, P. G. Huggard, D. R. Rusby, P. McKenna, C. M. Brenner, N. C. Woolsey, W. Wang, Z. Sheng, J. Zhang, *Proc. Natl. Acad. Sci. U. S. A.* **2019**, 116, 3994.
- [19] C. N. Santos, F. Joucken, D. De Sousa Meneses, P. Echegut, J. Campos-Delgado, P. Louette, J.-P. Raskin, B. Hackens, *Sci. Rep.* **2016**, 6, 24301.
- [20] S. Kovalev, R. M. A. Dantas, S. Germanskiy, J.-C. Deinert, B. Green, I. Ilyakov, N. Awari, M. Chen, M. Bawatna, J. Ling, F. Xiu, P. H. M. van Loosdrecht, P. Surówka, T. Oka, Z. Wang, *Nat. Commun.* **2020**, 11, 2451.
- [21] R. Matsunaga, N. Tsuji, H. Fujita, A. Sugioka, K. Makise, Y. Uzawa, H. Terai, Z. Wang, H. Aoki, R. Shimano, *Science* **2014**, 345, 1145.
- [22] A. von Hoegen, R. Mankowsky, M. Fechner, M. Först, A. Cavalleri, *Nature* **2018**, 555, 79.
- [23] M. Kozina, M. Fechner, P. Marsik, T. van Driel, J. M. Glowina, C. Bernhard, M. Radovic, D. Zhu, S. Bonetti, U. Staub, M. C. Hoffmann, *Nat. Phys.* **2019**, 15, 387.
- [24] M. C. Hoffmann, J. Hebling, H. Y. Hwang, K.-L. Yeh, K. A. Nelson, *J. Opt. Soc. Am. B* **2009**, 26, A29.
- [25] D. Nicoletti, A. Cavalleri, *Adv. Opt. Photonics* **2016**, 8, 401.
- [26] J. Hebling, M. C. Hoffmann, H. Y. Hwang, K.-L. Yeh, K. A. Nelson, *Phys. Rev. B: Condens. Matter Mater. Phys.* **2010**, 81, 035201.
- [27] X. C. Zhang, A. Shkurinov, Y. Zhang, *Nat. Photonics* **2017**, 11, 16.
- [28] L. Zhang, X. Q. Chen, S. Liu, Q. Zhang, J. Zhao, J. Y. Dai, G. D. Bai, X. Wan, Q. Cheng, G. Castaldi, V. Galdi, T. J. Cui, *Nat. Commun.* **2018**, 9, 4334.
- [29] H. Hirori, K. Shinokita, M. Shirai, S. Tani, Y. Kadoya, K. Tanaka, *Nat. Commun.* **2011**, 2, 594.
- [30] N. I. Zheludev, Y. S. Kivshar, *Nat. Mater.* **2012**, 11, 917.
- [31] M. Manjappa, P. Pitchappa, N. Singh, N. Wang, N. I. Zheludev, C. Lee, R. Singh, *Nat. Commun.* **2018**, 9, 4056.
- [32] P. Pitchappa, A. Kumar, S. Prakash, H. Jani, T. Venkatesan, R. Singh, *Adv. Mater.* **2019**, 31, 1808157.
- [33] M. Manjappa, A. Solanki, A. Kumar, T. C. Sum, R. Singh, *Adv. Mater.* **2019**, 31, 1901455.
- [34] W. J. Padilla, A. J. Taylor, C. Highstrete, M. Lee, R. D. Averitt, *Phys. Rev. Lett.* **2006**, 96, 107401.
- [35] K. Fan, H. Y. Hwang, M. Liu, A. C. Strikwerda, A. Sternbach, J. Zhang, X. Zhao, X. Zhang, K. A. Nelson, R. D. Averitt, *Phys. Rev. Lett.* **2013**, 110, 217404.
- [36] C. Lange, T. Maag, M. Hohenleutner, S. Baierl, O. Schubert, E. R. Edwards, D. Bougeard, G. Woltersdorf, R. Huber, *Phys. Rev. Lett.* **2014**, 113, 227401.
- [37] K. Iwaszczuk, M. Zalkovskij, A. C. Strikwerda, P. U. Jepsen, *Optica* **2015**, 2, 116.
- [38] M. A. Seo, H. R. Park, S. M. Koo, D. J. Park, J. H. Kang, O. K. Suwal, S. S. Choi, P. C. M. Planken, G. S. Park, N. K. Park, Q. H. Park, D. S. Kim, *Nat. Photonics* **2009**, 3, 152.
- [39] J.-Y. Kim, B. J. Kang, J. Park, Y.-M. Bahk, W. T. Kim, J. Rhie, H. Jeon, F. Rotermund, D.-S. Kim, *Nano Lett.* **2015**, 15, 6683.
- [40] T. Kang, R. H. J. Kim, G. Choi, J. Lee, H. Park, H. Jeon, C. H. Park, D. S. Kim, *Nat. Commun.* **2018**, 9, 4914.
- [41] S. Han, J.-Y. Kim, T. Kang, Y.-M. Bahk, J. Rhie, B. J. Kang, Y. S. Kim, J. Park, W. T. Kim, H. Jeon, F. Rotermund, D.-S. Kim, *ACS Photonics* **2016**, 3, 1440.
- [42] V. A. Fedotov, M. Rose, S. L. Prosvirnin, N. Papasimakis, N. I. Zheludev, *Phys. Rev. Lett.* **2007**, 99, 147401.
- [43] R. Singh, I. A. I. Al-Naib, M. Koch, W. Zhang, *Opt. Express* **2011**, 19, 6312.
- [44] X. Wu, B. Quan, X. Pan, X. Xu, X. Lu, C. Gu, L. Wang, *Biosens. Bioelectron.* **2013**, 42, 626.
- [45] L. Cong, M. Manjappa, N. Xu, I. Al-Naib, W. Zhang, R. Singh, *Adv. Opt. Mater.* **2015**, 3, 1537.
- [46] W. Cao, R. Singh, I. A. I. Al-Naib, M. He, A. J. Taylor, W. Zhang, *Opt. Lett.* **2012**, 37, 3366.
- [47] A. T. Tarekne, H. Hirori, K. Tanaka, K. Iwaszczuk, P. U. Jepsen, *New J. Phys.* **2017**, 19, 123018.
- [48] D. Laks, G. Neumark, S. Pantelides, *Phys. Rev. B: Condens. Matter Mater. Phys.* **1990**, 42, 5176.
- [49] A. Menikh, R. MacColl, C. A. Mannella, X. C. Zhang, *ChemPhysChem* **2002**, 3, 655.
- [50] Y. Monnai, K. Altmann, C. Jansen, H. Hillmer, M. Koch, H. Shinoda, *Opt. Express* **2013**, 21, 2347.
- [51] H. Guerboukha, K. Nallappan, M. Skorobogatiy, *Adv. Opt. Photonics* **2018**, 10, 843.
- [52] K. R. Jha, G. Singh, *Infrared Phys. Technol.* **2013**, 60, 71.
- [53] M. S. Sherwin, A. Imamoglu, T. Montroy, *Phys. Rev. A* **1999**, 60, 3508.